

1 **Dust pollution substantially weakens the impact of ammonia**
2 **emission reduction on particulate nitrate formation**

3 Hanrui Lang¹, Yunjiang Zhang^{1*}, Sheng Zhong², Yongcai Rao³, Minfeng Zhou⁴, Jian Qiu⁵, Jingyi Li¹, Diwen Liu⁶, Florian
4 Couvidat⁷, Olivier Favez⁷, Didier Hauglustaine⁸, Xinlei Ge¹

5 ¹Collaborative Innovation Center of Atmospheric Environment and Equipment Technology, Jiangsu Key Laboratory of
6 Atmospheric Environment Monitoring and Pollution Control, Nanjing University of Information Science and Technology,
7 Nanjing, China

8 ²Jiangsu Environmental Monitoring Center, Nanjing, China

9 ³Xuzhou Environmental Monitoring Center of Jiangsu, Xuzhou, China

10 ⁴Suzhou Environmental Monitoring Center of Jiangsu, Suzhou, China

11 ⁵Zhenjiang Environmental Monitoring Center of Jiangsu, Zhenjiang, China

12 ⁶Graduate School of Arts and Science, Columbia University, New York City, USA

13 ⁷Institut National de l'Environnement Industriel et des Risques, Verneuil-en-Halatte, France

14 ⁸Laboratoire des Sciences du Climat et de l'Environnement, CNRS-CEA-UVSQ, Université Paris-Saclay, Gif-sur-Yvette,
15 France

16 *Correspondence to:* Yunjiang Zhang (yjzhang@nuist.edu.cn)

17

18 **Abstract.** Dust emissions significantly influence air quality and contribute to nitrate aerosol pollution by altering aerosol
19 acidity. Understanding how dust interacts with ammonia emission controls is crucial for managing particulate nitrate
20 pollution, especially in urban areas. In this study, we conducted field measurements of aerosol components and gases
21 across three cities in Eastern China during the Spring of 2023. By combining an aerosol thermodynamic model with
22 machine learning, we assessed the contribution of dust to aerosol pH and its impact on nitrate formation. Our results show
23 that changes in ammonia, both in the gas and particle phases, were the main factors affecting aerosol pH, with dust
24 particles contributing to about 7% of the total pH variation. During dust events, high concentrations of non-volatile ions
25 increased aerosol pH, leading to higher nitrate levels in particulate phase. Machine learning analysis revealed that extreme
26 dust storms caused a significant change in aerosol pH, enhancing nitrate partitioning. Further simulations indicated that
27 while reducing ammonia emissions is effective in lowering nitrate levels under normal conditions, this effect is
28 significantly reduced in dust-affected environments. Dust particles act as a buffer, reducing the sensitivity of nitrate
29 formation to ammonia emission reductions. These findings emphasize the need to consider dust pollution when designing
30 strategies for controlling particulate nitrate levels and highlight the complex interactions between dust and anthropogenic
31 emissions.

32

1 Introduction

Airborne dust is a major component of atmospheric aerosols, accounting for approximately 75% of the global aerosol mass load (Mahowald et al., 2006; Zhao et al., 2022; Chen et al., 2023c). Dust exerts multiple impacts on air quality (Jickells et al., 2005; Rosenfeld et al., 2001), climate (Huang et al., 2011), and human health (Zhang et al., 2023; Goudie, 2014). It can be broadly categorized into anthropogenic dust and natural dust based on sources and emission mechanisms (Chen et al., 2018; Chen et al., 2023a). Anthropogenic dust originates from human activities, such as construction, agricultural and non-exhaust vehicular emissions (Liu et al., 2021). In contrast, natural dust mainly arises from bare surfaces in arid and semi-arid regions (Shao and Dong, 2006), which cover approximately 30% of the global land area (Soussé-Villa et al., 2024; Xin et al., 2023). Beyond anthropogenic influences, over 300 countries worldwide are affected by natural dust pollution (Kurokawa and Ohara, 2020; Notaro et al., 2015). Dust storms originating in arid regions can be transported over thousands of kilometers, significantly impacting downstream air quality and atmospheric chemistry (Tan et al., 2012; Milousis et al., 2024; Sun et al., 2001).

Dust emissions contain nonvolatile cations (NVCs), such as calcium and magnesium ions, which are alkaline substances that can neutralize acidic aerosol components, such as sulfates, thereby increasing aerosol pH (Wu et al., 2013; Ding et al., 2019). Dust particles also engage in heterogeneous reactions with gaseous nitric acid, buffering acidic species and modulating pH dynamics (Zhi et al., 2025). Aerosol pH is a critical factor in atmospheric chemical processes, influencing gas-particle partitioning of inorganic aerosols (Guo et al., 2018), secondary organic aerosol (SOA) formation (Xu et al., 2015; Zhang et al., 2017; Nguyen et al., 2014), and metal-catalyzed oxidation reactions (Fang et al., 2017). Regional variations in aerosol pH alter the chemical characteristics of atmospheric pollution, affecting pollutant lifetimes and deposition rates, which in turn have profound implications for ecosystems and public health (Guo et al., 2016). Despite the incorporation of aerosol pH modules in some atmospheric chemistry models, inaccuracies in dust emission inventories can lead to biases in estimated aerosol pH, thereby introducing systematic errors in simulating associated chemical processes, such as nitrate formation.

Nitrate has emerged as a dominant component of fine particulate matter (PM_{2.5}) worldwide (e.g., China, Europe, the United States, and India), particularly as sulfate aerosol concentrations decline due to sustained SO₂ emission reductions (Weber et al., 2016; Geng et al., 2017; Zhai et al., 2021; Hauglustaine et al., 2014; Beaudor et al., 2024). The reaction between gaseous nitric acid (HNO₃) and ammonia (NH₃) represents one of the primary pathways for the formation of fine mode nitrate (Stelson and Seinfeld, 1982; Metzger et al., 2002). Nitrate formation plays a critical role in atmospheric

chemistry and the global nitrogen cycle, including reactive nitrogen deposition (Chul H. Song, 2000). The gas-particle partitioning of HNO_3 and nitrate formation is strongly influenced by aerosol pH (Guo et al., 2018; Shi et al., 2019). When total ammonia (gaseous and particulate) or NVCs are insufficient to fully neutralize aerosol sulfate, HNO_3 will not condense on aerosol due to low pH (Nenes et al., 2020; Guo et al., 2017a; Vasilakos et al., 2018; Ding et al., 2019). However, this conceptual framework may oversimplify the influence of aerosol acidity, as it fails to fully consider the substantial volatility differences between deliquescent aerosols containing sulfates or NVCs and those dominated by ammonium or nitrate, both of which are highly sensitive to aerosol pH (Nenes et al., 2020; Nenes et al., 2021). In dust-polluted environments, however, the abundance of alkaline particles, such as calcium ions, can alter nitrate formation pathways (Seinfeld et al., 1998; Hrdina et al., 2021; Li et al., 2024). Quantitative insights into how urban dust influences nitrate formation and its regulation remain nevertheless limited.

East Asia, home to some of the world's major dust source regions, significantly contributes to global atmospheric dust pollution. Under the influence of Mongolian cyclones, dust particles originating from Mongolia are transported long distances, affecting air quality and atmospheric processes across East Asia (Fu et al., 2014; Sun et al., 2001; Wang et al., 2021; Xu et al., 2020). The Yangtze River Delta (YRD) is a densely urbanized region in Eastern China, where air quality is influenced by both natural and local anthropogenic dust sources. This region provides an ideal atmospheric experiment to investigate the impact of dust pollution on urban aerosol acidity and nitrate chemistry. Under these contexts, this study examines changes in aerosol pH, and nitrate gas-particle partitioning (defined as the gas-particle partitioning of HNO_3 combined to its acid dissociation) under influence of both anthropogenic and natural dust pollution in spring 2023, focusing on three representative cities (Xuzhou, Zhenjiang, and Suzhou) in the YRD. The contributions of chemical and meteorological components to aerosol pH and the effects of dust storms on $\epsilon(\text{NO}_3^-)$ are quantified. By integrating statistical analysis approaches, we further quantify the contribution of different factors to aerosol pH and $\epsilon(\text{NO}_3^-)$. Sensitivity analyses are conducted to evaluate the effects of TNH_x ($\text{TNH}_x = \text{NH}_3 + \text{NH}_4^+$), TNO_3 ($\text{TNO}_3 = \text{HNO}_3 + \text{NO}_3^-$) and SO_4^{2-} emission controls on nitrate partitioning across varying dust pollution levels, providing a scientific basis for formulating nitrate pollution control strategies during dust events.

2.Data and Methods

2.1 Sampling site and instruments

This study selected three cities in the YRD region, China, that represent a gradient of dust transport effects: Xuzhou

(32.18°N, 119.48°E), Zhenjiang (32.16°N, 119.49°E), and Suzhou (31.29°N, 120.61°E). These cities are distributed along the north-to-south dust transport pathway, enabling a systematic investigation of the impacts of dust transport, including gradient variations in particle chemical properties, aerosol acidity (pH), and gas–particle partitioning. The sampling sites comprehensively reflect the gradient effects of dust across different regions. These sampling sites are representative of typical urban environments and reflect the general atmospheric conditions within the region.

Water-soluble inorganic ions (e.g., NH_4^+ , Na^+ , K^+ , Ca^{2+} , Mg^{2+} , SO_4^{2-} , NO_3^- , Cl^-) in $\text{PM}_{2.5}$ and gaseous components (NH_3 , HNO_3 , HCl) were continuously measured using a Monitor for Aerosols and Gases in ambient Air (MARGA) system (Trebs et al., 2004; Rumsey et al., 2014). The system exhibited high correlation between cation and anion measurements (Fig. S1), indicating reliable performance. During the observation period, ambient air was continuously drawn into the MARGA system, where aerosols and gas-phase species were separated. Water-soluble gases were first removed using a wet rotating denuder. Subsequently, aerosol particles with aerodynamic diameters $\leq 2.5 \mu\text{m}$ were collected using a wet aerosol sampler, where they were dissolved in water to form a sample liquid that was then analyzed by ion chromatography (Rumsey et al., 2014; Trebs et al., 2004). For gaseous pollutants, air samples passed through a membrane filter to remove particles before entering a scrubbing tower, where gas-phase components were dissolved in water to form sample liquid for ion chromatographic analysis (Rumsey et al., 2014). The MARGA system is equipped with automatic calibration and cleaning functions, ensuring stability and accuracy during long-term operation. The entire process is controlled by dedicated software, enabling simultaneous monitoring of multiple components and real-time data output (Schaap et al., 2004).

Meteorological parameters data (air temperature and relative humidity) were obtained from corresponding observation stations, while additional meteorological parameters were sourced from the European Centre for Medium-Range Weather Forecasts (ECMWF) ERA5 reanalysis dataset (<https://cds.climate.copernicus.eu/>, last access: November 21, 2023). Regional PM_{10} data were retrieved from the China National Environmental Monitoring Centre (<https://air.cnemc.cn:18007/>, last access: November 21, 2023).

2.2 Aerosol pH estimation

Aerosol pH is a particle property that significantly influences aerosol formation, yet it is challenging to measure directly. Traditional methods, such as ion balance and molar ratio approaches, often fail to provide accurate evaluations of aerosol pH (Guo et al., 2016; Weber et al., 2016). Currently, the most widely used approaches include the E-AIM and

ISORROPIA-II thermodynamic model (Fountoukis and Nenes, 2007), while recent studies have also begun to explore alternative methods for direct pH measurement (Li et al., 2025). In this study, we employed the ISORROPIA-II thermodynamic model to estimate aerosol pH (see Eq. 1) as well as the gas–particle partitioning of water-soluble ions, semi-volatile compounds, and water content. At low RH, aerosols are unlikely to be in a completely liquid state, and secondary organic aerosols (SOA) may affect the distribution of semi-volatile compounds due to reduced diffusion within the particles, thus influencing the predicted pH values; At high RH levels, such as $RH > 95\%$, aerosols may deliquesce, and the exponential increase in water activity (W_i) can introduce significant uncertainty into the pH values (Guo et al., 2017; Malm and Day, 2001). To improve the model's accuracy, we applied both the forward mode for metastable aerosols and excluded data with relative humidity (RH) below 35% or above 95% (Nah et al., 2018; Guo et al., 2015). The equation used to calculate aerosol pH in ISORROPIA-II is as follows (Liu et al., 2022):

$$pH = -\log_{10} \frac{1000\gamma_{H^+}C_{H^+}}{W_i} \quad (1)$$

In the Eq. (1), γ_{H^+} represents the activity coefficient of hydrogen ions, which is generally set to 1 (Liu et al., 2022). C_{H^+} denotes the hydrogen ion concentration in the aerosol aqueous phase, expressed in $\mu\text{g m}^{-3}$. W_i refers to the water content of the aerosol phase output by ISORROPIA-II (in $\mu\text{g m}^{-3}$). By incorporating these parameters, the ISORROPIA-II model provides a reliable framework for estimating aerosol pH, allowing for accurate analysis of its variation and impact under different environmental and pollution scenarios, including those influenced by dust events.

2.3 The gas–particle partitioning of nitrate

Nitrate, owing to its volatility, exists in the atmosphere in two primary forms. In the particulate phase, it predominantly appears as semi-volatile ammonium nitrate. However, where ammonia and NVCs fail to fully neutralize aerosol sulfate, the formation of semi-volatile ammonium nitrate is inhibited. Under such conditions, nitrate tends to remain in the gaseous phase as HNO_3 , which can subsequently transform into more stable coarse-mode salts, such as $\text{Ca}(\text{NO}_3)_2$, over time (Guo et al., 2017c; Vasilakos et al., 2018; Hrdina et al., 2021). Gas–particle partitioning of nitrate [$\epsilon(\text{NO}_3^-)$] defined as the ratio between particle-phase nitrate over TNO_3 serves as a key indicator of nitrate distribution between its gaseous and particulate phases. Changes in aerosol pH, influenced by varying meteorological conditions, significantly affect $\epsilon(\text{NO}_3^-)$. This study employs Eq. (2) (Guo et al., 2018; Nenes et al., 2020) to calculate theoretical values of $\epsilon(\text{NO}_3^-)$ for each observational dataset. The results enable a detailed analysis of how variations in pH across different ranges influence the gas–particle partitioning of nitrate.

$$\varepsilon(NO_3^-) = \frac{H_{HNO_3}^* W_i RT (0.987 \times 10^{-14})}{\gamma_{NO_3^-} \gamma_{H^+} 10^{-pH} + H_{HNO_3}^* W_i RT (0.987 \times 10^{-14})} \quad (2)$$

In the equation, $H_{HNO_3}^* = H_{HNO_3} K_{n1}$ ($\text{mol}^2 \text{kg}^{-2} \text{atm}^{-1}$) represent the product of the Henry's law constant and the acid dissociation constant for HNO_3 . R is the ideal gas constant ($\text{J mol}^{-1} \text{K}^{-1}$), and T is the temperature in Kelvin (K). The temperature dependence for H_{HNO_3} and K_{n1} can be found in Clegg et al. (1998). pH is calculated using Eq. (1). The factor 0.987×10^{-14} is a unit conversion factor used to convert from atm and μg to SI units. $\gamma_{NO_3^-}$ and γ_{H^+} are the activity coefficients for NO_3^- and H^+ , respectively. Activity coefficient predicted by ISORROPIA-II are $\gamma_{NO_3^-} \gamma_{H^+} = 0.28$, $\gamma_{H^+} = 1$ (Guo et al., 2018; Guo et al., 2017b; Nah et al., 2018). In the standard S-curve, pH varies within a specific range, and this relationship is influenced by the temperature dependence of the Henry's law constant and the acid dissociation constant. This model allows for a more accurate estimation of nitrate aerosol behavior under varying environmental conditions. More detailed information about inputs and outputs for the ISORROPIA-II model can be found in Tables S1 – S3.

2.4 Multi-site concentration weighted trajectory

The concentration weighted trajectory (CWT) analysis is widely used to assess the potential origins and transport pathways of air pollutants observed at receptor sites. By integrating trajectory analysis, this approach provides insights into pollutant sources and their atmospheric transport dynamics. In this study, we employed the CWT model, coupled with backward trajectories and multi-site air quality monitoring data, to investigate the potential source regions and long-range transport of the spring 2023 dust storm event observed in Xuzhou, Zhenjiang, and Suzhou. When combined with data from multiple monitoring sites, the CWT model demonstrates enhanced robustness and reliability (Boichu et al., 2019). Briefly, multi-site CWT analysis integrates pollutant concentration data from several monitoring stations with the corresponding backward trajectories to estimate the likely origins of the observed pollutants. Air pollutant concentrations are spatially allocated to grid cells traversed by air masses, weighted by the residence time within each grid cell. Compared to single-site CWT analysis, the multi-site approach offers broader spatial coverage, minimizes site-specific biases, and increases the dataset size, thereby improving the accuracy and spatial resolution of source apportionment, particularly for complex transport patterns.

In this study, 48-hour backward trajectories at 50 meters above ground level were computed using meteorological data from the Global Data Assimilation System (GDAS). The CWT analysis was conducted using the Zefir toolkit implemented in Igor Pro (Petit et al., 2017). This methodology provided a comprehensive assessment of dust transport and source attribution, facilitating a deeper understanding of dust storm dynamics in the region.

$$CWT_{ij} = \frac{\sum_{l=1}^n C_l \tau_{ij,l}}{\sum_{l=1}^n \tau_{ij,l}} \quad (3)$$

In Eq. (3), CWT_{ij} represents the weighted concentration in the grid at the i row and j column, C_l is the pollutant concentration corresponding to the l trajectory, and $\tau_{ij,l}$ is the residence time of the trajectory in the (i,j) grid. n denotes the total number of all trajectories.

2.5 Machine learning model

Aerosol pH and $\varepsilon(\text{NO}_3^-)$ exhibit nonlinear responses to multiple influencing factors. In this study, we employed a machine learning approach to investigate the effects of extreme dust storm conditions on aerosol pH and $\varepsilon(\text{NO}_3^-)$. Specifically, we used the random forest (RF) algorithm to construct regression models tailored to aerosol pH and $\varepsilon(\text{NO}_3^-)$ for each city under investigation. The dataset for the RF regression models was divided into a training set (80%) and a test set (20%). The training set was utilized to build the models, while the test set was used to validate their performance. The input predictive features for both aerosol pH and $\varepsilon(\text{NO}_3^-)$ models included the water-soluble inorganic chemical composition of aerosols (Na^+ , SO_4^{2-} , NH_4^+ , NO_3^- , Cl^- , Ca^{2+} , K^+ , Mg^{2+}), gaseous species (NH_3 and HNO_3), and meteorological parameters (T and RH). To evaluate the model performance, we applied 5-fold cross-validation for parameter tuning. Model performance was evaluated using seven statistical metrics: Mean Absolute Error (MAE), Root Mean Squared Error (RMSE), Normalized Mean Squared Error (NMSE), Mean Bias (MB), Normalized Mean Bias (NMB), Index of Agreement (IOA), and the correlation coefficient (R). Detailed definitions and calculations for these metrics are provided in Supplementary Text 1. This machine learning based approach enabled us to quantify the complex, nonlinear relationships between aerosol properties, chemical compositions, and meteorological conditions, offering deeper insights into the drivers of aerosol pH and $\varepsilon(\text{NO}_3^-)$ under varying dust pollution scenarios.

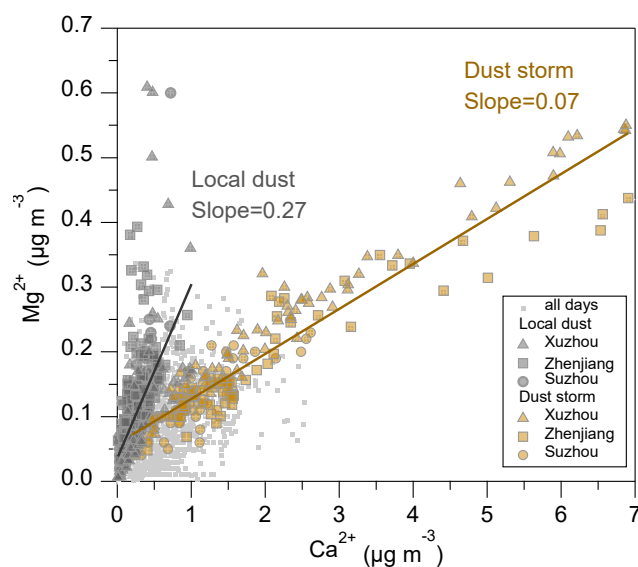
In addition, SHapley Additive exPlanations (SHAP), a method derived from the Shapley value concept in game theory, provides an interpretable framework to explain the predictions of complex machine learning models. SHAP quantifies the contribution of each input variable to individual predictions, making it a powerful tool for understanding model behavior (Duan et al., 2024; Lundberg and Lee, 2017). In this study, SHAP values were employed to assess the influence of various factors on aerosol pH and $\varepsilon(\text{NO}_3^-)$ under dust storm and local dust conditions. A positive SHAP value for a given factor indicates that it contributes positively to the prediction, whereas a negative SHAP value implies a suppressive or inhibitory impact. This analysis allowed us to disentangle the relative contributions of chemical composition, meteorological conditions, and other variables to the variations in aerosol properties under different dust

196 scenarios.

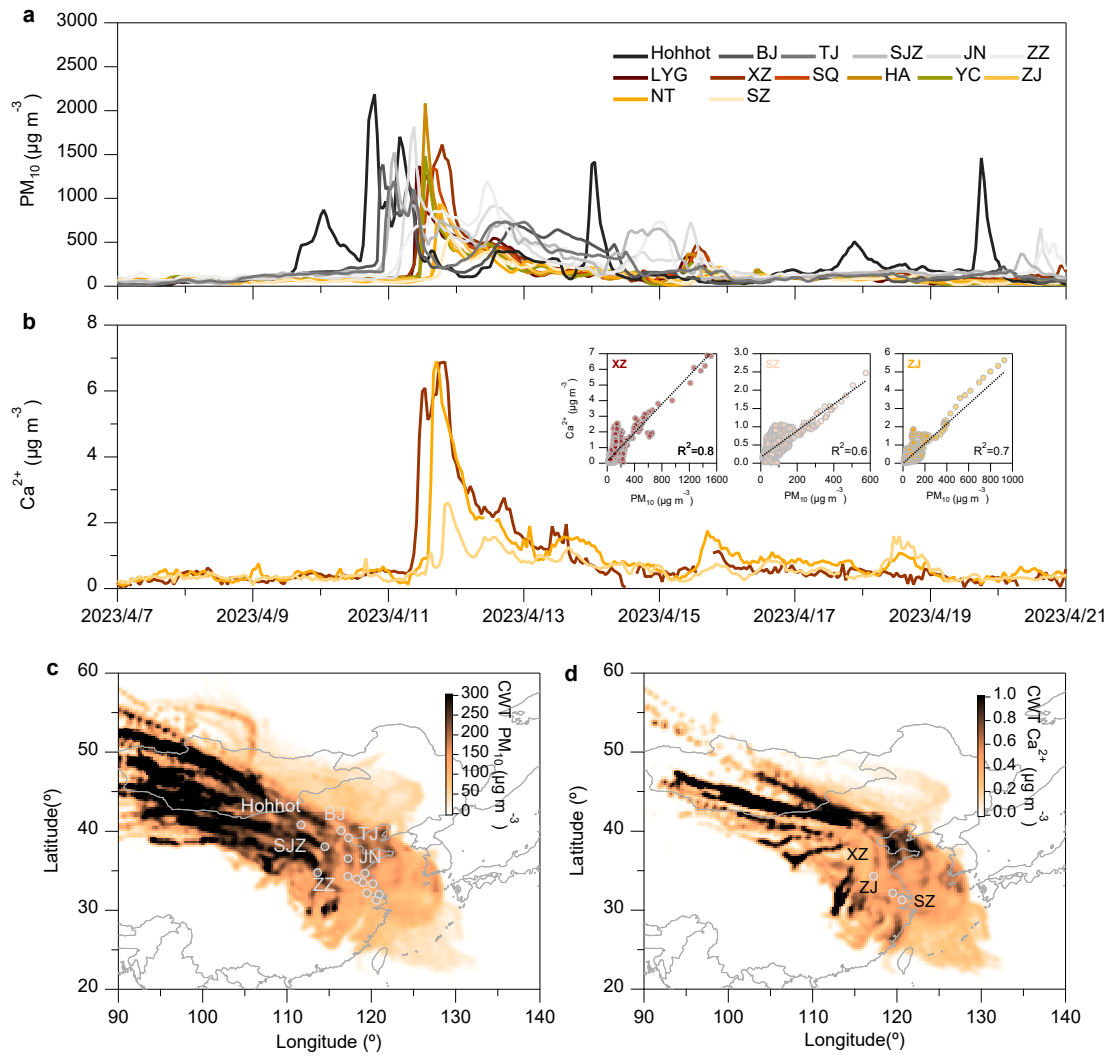
197 3. Results and Discussion

198 3.1 Observational evidence of anthropogenic and natural dust pollution

199 Dust emissions can be classified into anthropogenic and natural sources, with Ca^{2+} and Mg^{2+} commonly used as
 200 tracers. Figure 1 shows the relationship between the concentrations of Ca^{2+} and Mg^{2+} during the observation period from
 201 March to April 2023 across the three cities (Xuzhou, Zhenjiang, and Suzhou). It is evident that the concentrations of Ca^{2+}
 202 and Mg^{2+} exhibit two distinctly different linear slopes, indicating that the different dust origins during this period were
 203 influenced by both long-range transport dust storms and local dust emissions. In particular, during the period from April
 204 11th to 13th, a severe dust storm originating was transmitted from northern regions, first impacting Hohhot, and then
 205 southward to the southern cities of the YRD region. As shown in Fig. 2a, the PM_{10} concentrations in the cities along the
 206 transport path exhibited a distinct gradient, with peak values reaching approximately $1702 \mu\text{g m}^{-3}$ in Hohhot, $1614 \mu\text{g}$
 207 m^{-3} in Xuzhou, $925 \mu\text{g m}^{-3}$ in Zhenjiang, and $576 \mu\text{g m}^{-3}$ in Suzhou, respectively. In Xuzhou, the average concentration
 208 of Ca^{2+} increased from $0.47 \pm 0.36 \mu\text{g m}^{-3}$ during the local dust period to $2.00 \pm 1.66 \mu\text{g m}^{-3}$ during the dust storm period,
 209 marking a fourfold increase. Similarly, the average Ca^{2+} concentration rose from $0.30 \pm 0.23 \mu\text{g m}^{-3}$ to $1.69 \pm 1.41 \mu\text{g m}^{-3}$
 210 in Zhenjiang, while the concentration increased from $0.35 \pm 0.26 \mu\text{g m}^{-3}$ to $0.92 \pm 0.52 \mu\text{g m}^{-3}$ in Suzhou.



211
 212 **Figure 1.** Relationship between Ca^{2+} and Mg^{2+} concentrations in $\text{PM}_{2.5}$ in Xuzhou (triangle), Zhenjiang (square), and Suzhou (circle).
 213 Dust types are distinguished based on the slope of the Ca^{2+} to Mg^{2+} concentration ratio, with local dust (gray) and dust storm (brown)
 214 indicated. Light gray dots represent the concentrations of Ca^{2+} and Mg^{2+} observed in the three cities during March – April 2023.



215

216 **Figure 2.** Time series of PM_{10} and Ca^{2+} concentrations, and their concentration-weighted trajectories for cities along the dust transport
 217 path. **(a)** Time series of PM_{10} in 14 cities along the BTH region, and **(b)** Time series of Ca^{2+} concentrations in Xuzhou, Zhenjiang, and
 218 Suzhou and the correlation of Ca^{2+} and PM_{10} . **(c)** 48-hour CWT-weighted spatial distribution of PM_{10} concentrations in 14 cities from
 219 April 5 to 20, and **(d)** 48-hour CWT-weighted spatial distribution of Ca^{2+} concentrations in Xuzhou, Zhenjiang, and Suzhou (units: $\mu\text{g m}^{-3}$).
 220 m^{-3}).

221

222 Figure 2a and b illustrate the temporal evolution of PM_{10} and Ca^{2+} concentrations during the dust storm, showing an
 223 initial spike in Hohhot, followed by a gradual increase across the Beijing-Tianjin-Hebei (BTH) region, and eventual
 224 dispersion into several cities in Jiangsu Province. This progression is consistent with the CWT-weighted trajectory
 225 patterns shown in Fig. 2c and d, which delineate the transport pathways of the dust storm. The maps highlight significant
 226 contributions from Mongolia – the dust storm's origin – to regions including Hohhot, Beijing, Tianjin, Shijiazhuang, Jinan,
 227 Zhengzhou, and Jiangsu. This finding corroborates the results of Chen et al. (2023b), who attributed the dust storm to a

228 strong cold high-pressure system and cold front that transported substantial quantities of coarse dust aerosols southward
229 into the YRD region. Southward-moving cold fronts play a critical role in the diffusion and transport of atmospheric
230 pollutants. In arid and semi-arid regions, these storms mobilize large amounts of crustal elements, such as Ca^{2+} , with high
231 winds lifting dust from surface sources, including city streets, construction sites, and other exposed land areas (Ding et
232 al., 2019).

233 Figure 3 presents the relative contributions of water-soluble inorganic species (WSIS) within $\text{PM}_{2.5}$ during local dust
234 and dust storm periods in Xuzhou, Zhenjiang, and Suzhou. Across all three cities, the combined contribution of sulfate,
235 nitrate, and ammonium consistently accounted for over 80% of WSIS, highlighting the important role of secondary
236 inorganic aerosols in fine particulate pollution. Among these, nitrate was the most abundant species during both periods,
237 particularly during local dust events, with an average contribution ranging from 49.3% to 52.6%. However, during dust
238 storms, its relative contribution declined to 34.0 – 40.8%. In contrast, the relative contribution of sulfate increased, with
239 increments of 5.2%, 5.0%, and 6.7% observed in Xuzhou, Zhenjiang, and Suzhou, respectively. Similar trends in the
240 relative increase of sulfate and reduction of nitrate during dust events have also been widely reported in previous studies
241 (e.g., Song et al., 2023; Zhu et al., 2022). This shift in WSIS composition was likely influenced by both meteorological
242 conditions and chemical processes associated with dust. To evaluate this hypothesis, we constructed separate random
243 forest regression models for nitrate and sulfate concentrations, using meteorological parameters (Table S4) as input
244 predictors. SHAP analysis was then applied to quantify the aggregated contributions of dispersion-related variables, such
245 as winds and planetary boundary layer height. As shown in Fig. S2, nitrate exhibited a stronger response to dispersion
246 and dilution effects than sulfate, indicating its higher sensitivity to meteorological variability during the dust storm. In
247 addition to meteorological effects, heterogeneous reactions involving mineral dust also likely influence the observed
248 variations in WSIS. For instance, previous studies have shown that the abundance of such nitrate-coated particles
249 increases with dust transport distance due to their relatively low deliquescence relative humidities, which facilitate nitric
250 acid uptake under humid conditions (Li and Shao, 2009; Tobo et al., 2010; Laskin et al., 2005). Given the widespread
251 presence of calcite and dolomite in Asian dust, long-range transported particles during dust storms provide abundant
252 alkaline surfaces for heterogeneous nitrate formation (Li and Shao, 2009). Consistent with this, our results showed an
253 average increase of approximately 10% in the relative contributions of Ca^{2+} and Mg^{2+} during the dust storm period across
254 all three cities compared to local dust events. This enhancement in alkaline mineral content suggests more effective
255 neutralization of acidic species such as HNO_3 and H_2SO_4 , thereby promoting the formation of particulate nitrate and

sulfate during dust transports (Li and Shao, 2009; Tobo et al., 2010; Laskin et al., 2005; Vasilakos et al., 2018; Guo et al., 2018). While secondary chemical formation was possible, meteorological dispersion and dilution appear to be the dominant factors leading to the observed concentration decreases. Nevertheless, further quantitative analysis of these factors requires comprehensive aerosol chemical measurements and atmospheric chemical transport modeling in future studies.

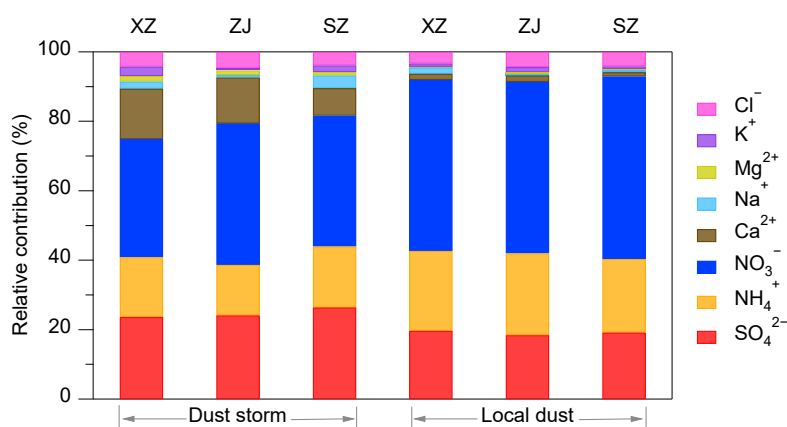


Figure 3. Relative contributions of water-soluble inorganics (SO_4^{2-} , NH_4^+ , NO_3^- , Ca^{2+} , Na^+ , Mg^{2+} , K^+ , and Cl^-) within the $\text{PM}_{2.5}$ fraction in Xuzhou, Zhenjiang, and Suzhou during dust storm and local dust pollution periods, respectively.

3.2 Driving factors of aerosol pH

Aerosol pH plays a crucial role in influencing aerosol formation and chemical composition. By regulating the partitioning of semi-volatile compounds between the gas and particle phases, aerosol pH directly affects the distribution of particulate matter in the atmosphere (Guo et al., 2017b). To examine the factors influencing aerosol pH, we utilized the ISORROPIA-II thermodynamic model and sensitivity analysis to quantify the relative contributions of chemical and meteorological factors, such as T and RH, in Xuzhou, Zhenjiang, and Suzhou. The correlation between simulated and observed concentrations of NH_3 and particulate NO_3^- is presented in Fig. 4. Across all three cities, the simulated values exhibit strong agreement with measurements ($R^2 = 0.94 - 0.99$). Additionally, Fig. S3 shows high correlations ($R^2 = 0.90 - 0.97$) for particle-phase ammonium and chloride between ISORROPIA-II predictions and observations, confirming the robust performance of the thermodynamic model in this study.

To assess the impact of individual factors (TNO_3 , TNH_x , Ca^{2+} , SO_4^{2-} , T and RH) on aerosol pH, we estimated their relative contributions using methods like those proposed by Zheng et al. (2020) and Zheng et al. (2022). First, we calculated the monthly average values for each factor in March and April, referred to as $\text{pH}_{i(3,3)}$ and $\text{pH}_{i(4,4)}$, respectively. Here, pH_i represents the influence of factor i on pH, with the numbers in parentheses indicating the respective months.

For example, for the analysis of a specific factor, we used the March average value of that factor while holding the other variables at their average levels for April. This yielded the aerosol pH value, denoted as $pH_{i(3,4)}$. Similarly, when using the April average value of the factor and maintaining the other variables at their March average levels, we recorded the resulting pH as $pH_{i(4,3)}$. The relative change in pH, denoted as $\Delta pH_{i(3)}$ and $\Delta pH_{i(4)}$ was calculated as the mean difference between $pH_{i(3,3)}$ and $pH_{i(4,3)}$, and between $pH_{i(4,4)}$ and $pH_{i(3,4)}$, respectively (see Eqs. 4 and 5). Finally, the overall impact of each factor on aerosol pH could be estimated (see Eq. 6).

$$\Delta pH_{i(3)} = pH_{i(3,3)} - pH_{i(4,3)} \quad (4)$$

$$\Delta pH_{i(4)} = pH_{i(4,4)} - pH_{i(3,4)} \quad (5)$$

$$\Delta pH_i = \frac{[\Delta pH_{i(3)}] + [\Delta pH_{i(4)}]}{2} \quad (6)$$

The impact of each factor could be positive or negative, which was detailed in Fig. S4. As shown in Fig. 5, atmospheric total ammonia emerged as the most significant driver of aerosol pH changes in all three cities, contributing 42%, 57%, and 43% of the observed pH in Xuzhou, Zhenjiang, and Suzhou, respectively. Total ammonia led to ΔpH_{TNH_x} increases of 0.6, 1.3, and 0.5 units in these cities during spring 2023. For Zhenjiang, T and Ca^{2+} were the next most influential factors, contributing 0.6 and 0.15 units to ΔpH_T and $\Delta pH_{Ca^{2+}}$, respectively. Sulfate exhibited the smallest influence on aerosol pH, where a concentration change of $0.3 \mu g m^{-3}$ corresponded to a $\Delta pH_{SO_4^{2-}}$ of approximately 0.05 units. These results align with the findings of Weber et al. (2016), which suggest that aerosol pH is less sensitive to changes in sulfate concentrations compared to ammonia levels.

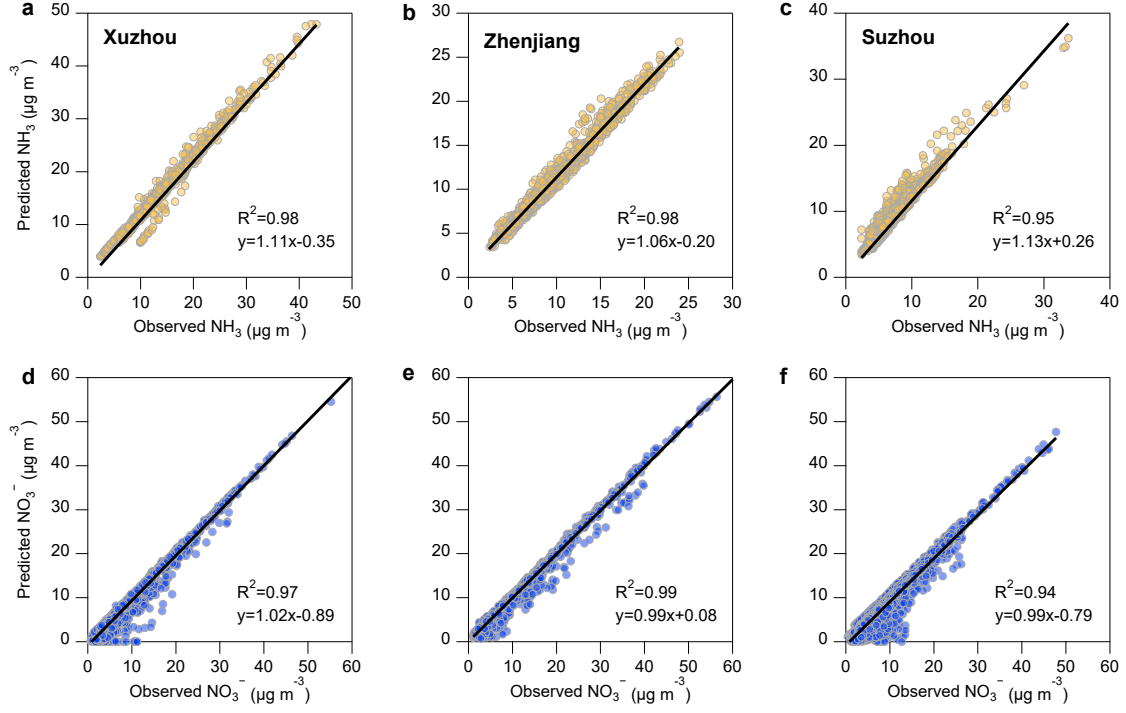


Figure 4. Correlation between ISORROPIA-II simulated and observed values of NH_3 and NO_3^- in three cities. (a) – (c) show the correlation between NH_3 predictions and observations, while (d) – (f) show the correlation between NO_3^- predictions and observations. The first column represents Xuzhou, the second column represents Zhenjiang, and the third column represents Suzhou.

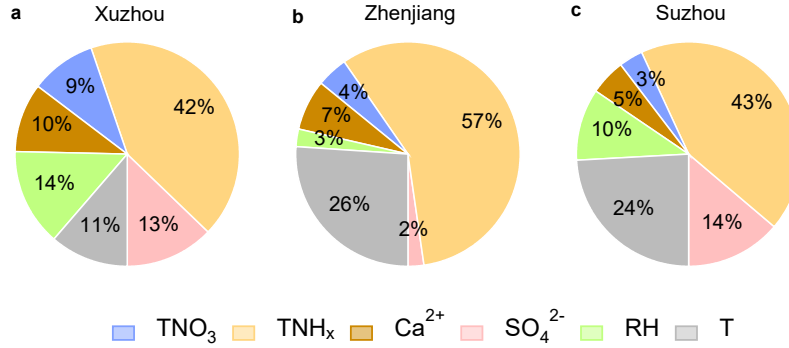
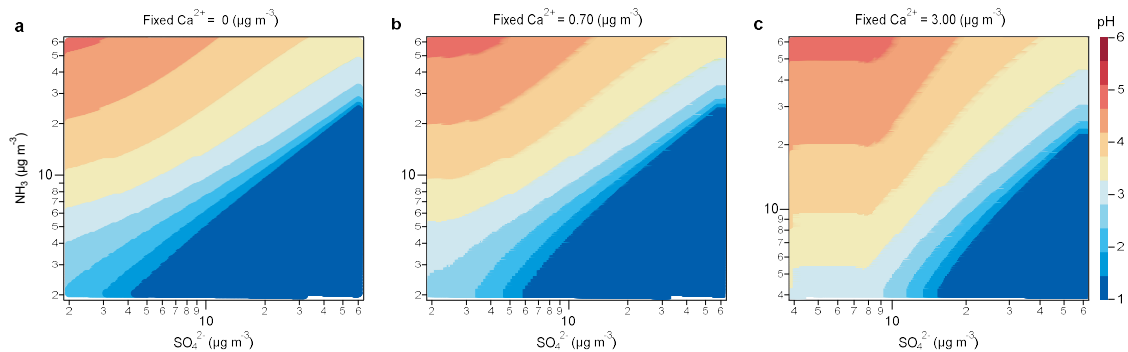


Figure 5. Relative contribution of different factors, including $\text{TNO}_3 = \text{HNO}_3 + \text{NO}_3^-$, $\text{TNH}_x = \text{NH}_3 + \text{NH}_4^+$, Ca^{2+} , SO_4^{2-} , RH, and T, to aerosol pH during the entire observation period in (a) Xuzhou, (b) Zhenjiang, and (c) Suzhou.

To further explore the response of aerosol pH to variations in SO_4^{2-} and NH_3 concentrations under different dust conditions (non-dust, local dust, and extremely dust storm), we conducted sensitivity simulations constrained by observations from Zhenjiang as a case study. As illustrated in Fig. 6a – c, we extended the NH_3 and SO_4^{2-} concentration ranges beyond their observed values to encompass potential variations across the YRD region. The input concentrations of Na^+ , SO_4^{2-} , total chloride ($\text{TCl}_x = \text{Cl}^- + \text{HCl}$), K^+ , and Mg^{2+} were fixed at the average levels observed in Zhenjiang

308 during the study period (see Table S2). Simulations were carried out under three distinct Ca^{2+} concentration scenarios: (1)
 309 non-dust ($\text{Ca}^{2+} = 0 \mu\text{g m}^{-3}$), (2) local dust ($\text{Ca}^{2+} = 0.7 \mu\text{g m}^{-3}$), and (3) extremely dust storm ($\text{Ca}^{2+} = 3.00 \mu\text{g m}^{-3}$). In these
 310 simulations, total ammonia ($\text{TNH}_x = \text{NH}_4^+ + \text{NH}_3$) and total nitrate ($\text{TNO}_3 = \text{NO}_3^- + \text{HNO}_3$) concentrations were
 311 independently changed and input into the ISORROPIA-II model. Under non-dust conditions ($\text{Ca}^{2+} = 0 \mu\text{g m}^{-3}$), the model
 312 predicted lower aerosol pH values. As shown in Fig. 6a – b, a 5 – 10-fold increase in NH_3 concentration led to a pH
 313 increase of approximately 1 unit, whereas aerosol pH demonstrated limited sensitivity to SO_4^{2-} concentration changes.
 314 This finding is consistent with previous studies (Zheng et al., 2022; Weber et al., 2016; Xie et al., 2020). However, under
 315 high Ca^{2+} concentration conditions, such as during extremely dust storm events, the influence of NH_3 on aerosol pH was
 316 notably mitigated (Fig. 6c). At relatively low SO_4^{2-} concentrations (i.e., below approximately $8 \mu\text{g m}^{-3}$, as indicated in
 317 Fig. 6c), aerosol pH exhibited diminished sensitivity to SO_4^{2-} levels, while showing greater responsiveness to variations
 318 in NH_3 . This behavior is modulated by the buffering capacity of Ca^{2+} , which preferentially reacts with SO_4^{2-} before
 319 interacting with NH_3 (Vasilakos et al., 2018), thereby limiting sulfate's ability to regulate aerosol acidity. These findings
 320 highlight that Ca^{2+} , a prominent component of mineral dust, plays a critical buffering role in mitigating the influence of
 321 NH_3 and SO_4^{2-} on aerosol acidity under dust-influenced atmospheric environments.



322 **Figure 6.** Sensitivity of the pH to ammonia (NH_3) and sulfate (SO_4^{2-}) concentrations based on ISORROPIA-II model predictions under
 323 different Ca^{2+} concentration conditions: (a) 0, (b) 0.70, and (c) $3.00 \mu\text{g m}^{-3}$.
 324

325

326 3.3 Impact of aerosol pH on the partitioning of nitric acid

327 In eastern China, nitrate has become a key component of $\text{PM}_{2.5}$, instead of sulfate (Xu et al., 2023; Gao et al., 2023).
 328 As a semi-volatile compound, nitrate is strongly influenced by the gas-particle partitioning process in the atmosphere.
 329 Aerosol pH not only determines the stability of nitrate but also governs whether it exists in the particulate phase or
 330 volatilizes as HNO_3 in the gas phase (Guo et al., 2018). At higher pH, nitrate tends to exist in the particle phase due to the

331 oxidation of NO_x , while under lower pH conditions, nitrate is more likely to volatilize into the gas phase as HNO_3 (Nenes
332 et al., 2020). Using Eq. (2), we analyzed the relationship between the nitrate particle-phase fraction ($\varepsilon(\text{NO}_3^-)$) and aerosol
333 pH for three cities – Xuzhou, Zhenjiang, and Suzhou – under dust storm and local dust conditions. Fig. 7 shows the S-
334 shaped curve representing this relationship, calculated based on the average T and aerosol W_i during dust storm and local
335 dust conditions, assuming ideal solution behavior (activity coefficient $\gamma_{H^+} = 1$). This curve visually demonstrates the
336 regulation of nitrate phase partitioning by aerosol pH under these conditions and provides a theoretical basis for
337 controlling the effect of ammonia on particulate nitrate formation by adjusting aerosol pH (Guo et al., 2018).

338 As cities along the dust storm transport path, Xuzhou, Zhenjiang, and Suzhou experience varying degrees of dust
339 influence, leading to significant differences in aerosol pH. On average, aerosol pH is elevated during dust storms
340 compared to local dust conditions. During non-dust periods, aerosol pH values in the three cities were significantly lower
341 than during dust events (Xuzhou: 2.7–4.0, Zhenjiang: 2.2–3.7, Suzhou: 2.0–3.6). This lower pH corresponds to a marked
342 decrease in $\varepsilon(\text{NO}_3^-)$, indicating a shift toward gaseous HNO_3 , especially in Suzhou where $\varepsilon(\text{NO}_3^-)$ dropped to
343 approximately 40% under the lowest pH conditions. During dust storms, the mean aerosol pH values were 5.50 ± 1.65 in
344 Xuzhou, 5.44 ± 1.69 in Zhenjiang, and 5.30 ± 1.67 in Suzhou. Under local dust conditions, these values were lower, at
345 4.12 ± 0.52 , 3.92 ± 0.32 , and 3.74 ± 0.69 respectively. Xuzhou, situated at the northern edge of the dust storm transport
346 path, exhibited the highest aerosol pH during both periods, reflecting the substantial impact of transported dust pollution.
347 The S-shaped curve in Fig. 7 demonstrates that under both dust storm and local dust conditions, the average aerosol pH
348 aligns with nitrate particle-phase fractions exceeding 99%, indicating that nitrate predominantly resides in the particle
349 phase. This finding highlights the promoting effect of dust pollution on the gas-to-particle transformation of nitrate.

350 When aerosol pH drops below 3, however, $\varepsilon(\text{NO}_3^-)$ decreases sharply, signifying the onset of nitrate volatilization
351 into the gas phase. Notably, when aerosol pH lies in the range of 1 to 3, $\varepsilon(\text{NO}_3^-)$ exhibits heightened sensitivity to aerosol
352 pH changes. This trend was consistently observed across all three cities. Reducing NH_3 concentrations is particularly
353 effective in influencing nitrate gas-particle partitioning when aerosol pH is within this sensitive range, offering a
354 promising strategy to mitigate regional particulate nitrate pollution. However, environments with dust pollution may
355 disrupt this theoretical relationship. NVCs (such as Ca^{2+}) in dust can neutralize acidic aerosol components, maintaining
356 aerosol pH at relatively high levels (e.g., $\text{pH} > \text{approximately } 3.5$) (Fig. 7). This neutralization effect limits the ability to
357 lower particulate nitrate concentrations solely by reducing NH_3 emissions, necessitating alternative approaches to address
358 nitrate-driven air quality challenges in dust-influenced regions.

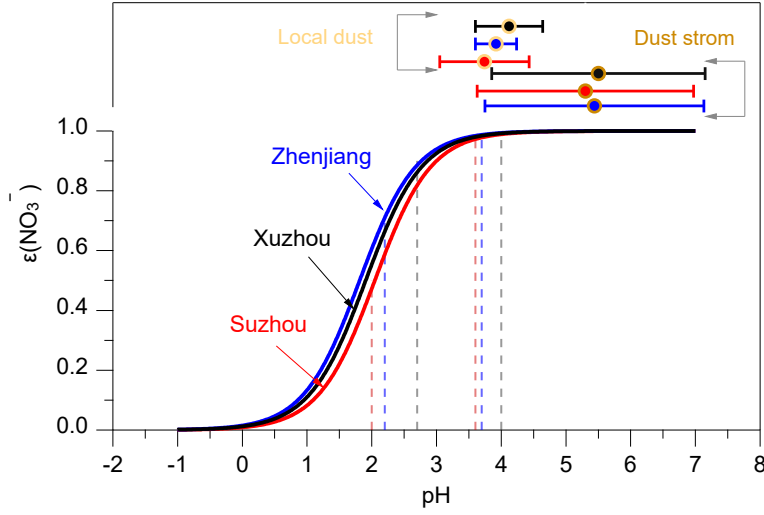
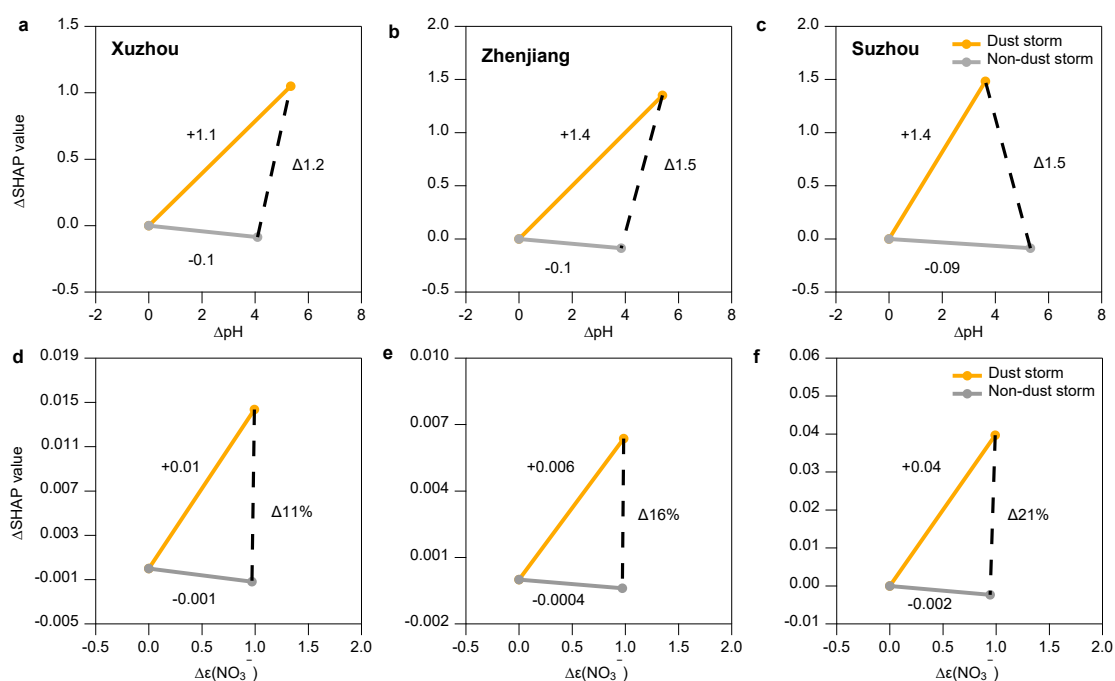


Figure 7. S-curve distributions for $\epsilon(\text{NO}_3^-)$ under the conditions from different cities. Based on Eq. (2), the relationship between $\epsilon(\text{NO}_3^-)$ and pH was calculated using the average T and W_i during dust storm, local dust and non-dust periods (assuming $\gamma_{\text{NO}_3^-}\gamma_{\text{H}^+}=0.28$, $\gamma_{\text{H}^+}=1$). The vertical dashed lines represent the minimum (left side) and maximum (right side) pH values under local-dust conditions calculated using ISORROPIA-II for the three cities. Error bars indicate the sample standard deviation of aerosol pH during local dust and dust storm events.

To further quantify the impact of dust storms on aerosol pH and $\epsilon(\text{NO}_3^-)$, we utilized the RF model combined with SHAP values for both prediction and sensitivity analysis. The correlation between the observed and predicted results from the RF model is shown in Fig. S5. The Index of Agreement (IOA) values ranged from 0.93 to 0.97, indicating a high level of model agreement. Meanwhile, the correlation coefficients (R) varied between 0.78 and 0.90, further validating the model's predictive accuracy. For aerosol pH predictions, five evaluation metrics were used: MAE, RMSE, NMSE, MB, and NMB. The values for MAE ranged from 0.13 to 0.18, while RMSE values were between 0.26 and 0.29. For NMSE, the values ranged from 0.10 to 0.12, and the biases (MB and NMB) varied from -0.01 to -0.006 and 0.004 to 0.007, respectively. In comparison, the corresponding evaluation metrics for $\epsilon(\text{NO}_3^-)$ were as follows: MAE ranged from 0.01 to 0.02, RMSE from 0.03 to 0.04, and NMSE from 0.10 to 0.21. The bias values for $\epsilon(\text{NO}_3^-)$ ranged from -0.00006 to 0.004 for MB and from 0.003 to 0.007 for NMB. These statistical results demonstrate the reliability and robustness of the RF model in predicting aerosol pH and nitrate partitioning.

Figure 8 illustrates the impact of dust storms and local dust conditions on aerosol pH and $\epsilon(\text{NO}_3^-)$. The ΔSHAP values represent the difference between the average SHAP values of all variables during dust storm periods and the average SHAP values for all variables during the non-dust storm period. During dust storm conditions, ΔSHAP significantly increased in Xuzhou, Zhenjiang, and Suzhou, with aerosol pH values rising by $\Delta 1.2$, $\Delta 1.5$, and $\Delta 1.5$ units,

381 respectively (Fig. 8 a-c). This result is consistent with our previous conclusion that dust storms contribute to an increase
 382 in aerosol pH, confirming the positive impact of dust storms on the random forest model's predictions of aerosol pH.
 383 Similarly, Fig. 8 d-f shows the changes in $\varepsilon(\text{NO}_3^-)$ for the three cities under different weather conditions. It is evident that
 384 the effect of dust storms on $\varepsilon(\text{NO}_3^-)$ is 10 to 20 times greater than the impact of local non-dust storm conditions, likely
 385 due to differences in aerosol composition and enhanced alkaline inputs such as Ca^{2+} . This indicates that dust storm
 386 conditions have a significantly stronger positive contribution to the particle-phase fraction of nitrate. The presence of
 387 dust particles facilitates the conversion of nitrate to the particulate phase, highlighting the significant influence of dust
 388 storms on nitrate partitioning in the atmosphere.



389
 390 **Figure 8.** Δ SHAP values for (a) – (c) aerosol pH and (d) – (f) $\varepsilon(\text{NO}_3^-)$. The orange solid line represents the impact of dust storms, the
 391 gray solid line represents the non-dust scenario, and the black dashed line shows the difference between the two scenarios.

392 393 3.4 Effectiveness of emission reduction on particulate nitrate under dust pollution

394 To explore the impact of emission reductions of TNH_x , TNO_3 , and SO_4^{2-} on $\varepsilon(\text{NO}_3^-)$ during different dust storm
 395 conditions, we conducted a sensitivity analysis based on the thermodynamic model ISORROPIA-II, using the average
 396 pollutant concentrations observed in Zhenjiang during the spring of 2023. The results, shown in Fig. 9, demonstrate a
 397 nonlinear response of both $\varepsilon(\text{NO}_3^-)$ and the total ammonium-nitrate concentration ($\text{NH}_4^+ + \text{NO}_3^-$) to reductions in TNH_x ,
 398 TNO_3 , and SO_4^{2-} , respectively. We simulated the effects of progressively reducing TNH_x , TNO_3 , and SO_4^{2-} by 0% to 50%

399 under different Ca^{2+} concentration conditions, which include different dust pollution scenarios. For the simulation, Ca^{2+}
400 concentration was set to 0.1 to 0.7 $\mu\text{g m}^{-3}$ for local dust conditions and ranged from 1.0 to 3.0 $\mu\text{g m}^{-3}$ for dust storm
401 conditions. When the Ca^{2+} concentration exceeded 3 $\mu\text{g m}^{-3}$, further reductions in the other variables had negligible effects
402 on the output, with emission reductions having little to no impact on $\epsilon(\text{NO}_3^-)$.

403 As shown in Fig. 9a, it is evident that during local dust conditions, $\epsilon(\text{NO}_3^-)$ remained relatively constant until TNH_x
404 emissions were reduced by 30%. At this point, $\epsilon(\text{NO}_3^-)$ rapidly dropped from 99%, signaling the onset of a significant
405 shift in the gas-particle partitioning of nitrate. When TNH_x reductions reached 50%, $\epsilon(\text{NO}_3^-)$ fell sharply to approximately
406 30%, indicating that nitrate transitioned predominantly into its gas-phase form. This simulation result is consistent with
407 the sensitivity analysis of NH_3 concentrations in section 3.2, which also showed a significant response in nitrate
408 partitioning as NH_3 concentrations decreased. Thus, in the Zhenjiang region, a 30% reduction in TNH_x emissions is
409 necessary to effectively reduce the mass of $(\text{NH}_4^+ + \text{NO}_3^-)$ during spring (Fig. 10d). In contrast, during dust storm
410 conditions (Fig. 9a), the reduction in TNH_x had a much more subdued effect on $\epsilon(\text{NO}_3^-)$, especially at higher Ca^{2+}
411 concentrations (above 2.5 $\mu\text{g m}^{-3}$), where the reduction had almost no impact on $\epsilon(\text{NO}_3^-)$.

412 For TNO_3 reductions, as shown in Fig. 10 b, the changes in $\epsilon(\text{NO}_3^-)$ were minimal, regardless of the Ca^{2+}
413 concentration. However, during local dust conditions (Fig. 9e), the reduction of TNO_3 led to a significant decrease in
414 $(\text{NH}_4^+ + \text{NO}_3^-)$ concentrations, indicating that TNO_3 reduction was particularly effective under local dust conditions.
415 Lastly, reductions in SO_4^{2-} emissions (Fig. 9c and f) had a smaller impact on both $\epsilon(\text{NO}_3^-)$ and $(\text{NH}_4^+ + \text{NO}_3^-)$
416 concentrations. Interestingly, at very low dust concentrations, SO_4^{2-} reductions could even lead to a slight increase (by up
417 to 0.5%) in $\epsilon(\text{NO}_3^-)$, indicating that sulfate reduction alone is not an effective strategy for controlling nitrate partitioning.

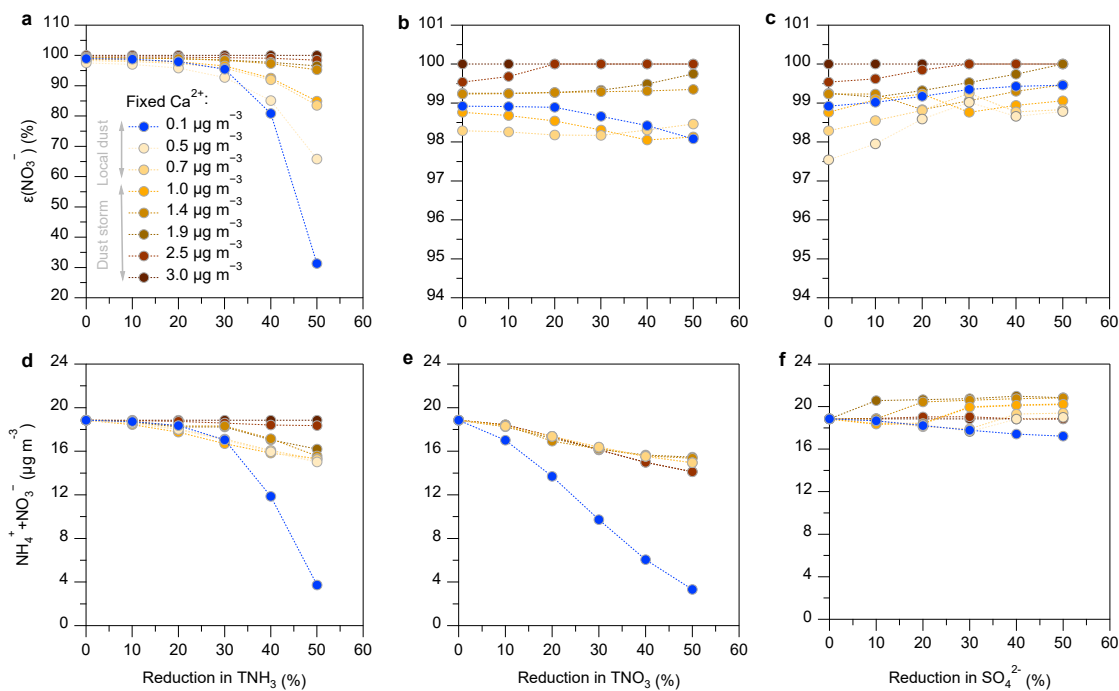


Figure 9. Sensitivity analysis based on the thermodynamic model ISORROPIA-II simulated the impact of reducing TNH_x ($\text{TNH}_x = \text{NH}_3 + \text{NH}_4^+$), TNO_3 ($\text{TNO}_3 = \text{HNO}_3 + \text{NO}_3^-$), and SO_4^{2-} by 0-50% during dust events of varying intensities on $\epsilon(\text{NO}_3^-)$ and $\text{NH}_4^+ + \text{NO}_3^-$.

4. Conclusions and Impactions

This study explores the impact of dust pollution on aerosol pH and nitrate gas-particle partitioning in three cities across the YRD region of Eastern China. By combining field observations, thermodynamic modeling, and machine learning techniques, we provide a comprehensive analysis of how different dust scenarios affect urban aerosol pH and gas-particle partitioning chemistry of nitrate. Our analysis of a dust storm event that originated in Mongolia and was transported over long distances to the YRD region in the spring of 2023 revealed a significant increase in PM_{10} concentrations, the average PM_{10} concentration in three cities along the route exceeds $400 \mu\text{g m}^{-3}$, approximately four times higher than during local dust events. Thermodynamic simulations using the ISORROPIA model showed that both ammonia and calcium ion concentrations strongly influenced aerosol pH, with average contributions of 47% and 7% respectively. Random forest model simulations further indicated that the presence of high NVCs during dust storms significantly contributed to changes in aerosol pH (1.2 – 1.5 units). Sensitivity analysis of pH responses to sulfate and NH_3 concentrations under different dust conditions (non-dust, local dust, and extremely dust storm) revealed that a 5 to 10 fold increase in NH_3 led to a 1-unit change in aerosol pH. Machine learning analysis showed that extreme dust storm events contributed approximately 1.4 units to the increase in aerosol pH, with a corresponding increase in nitrate

436 partitioning (16%). This suggests that under high aerosol pH conditions during dust pollution periods, nitrate is
437 predominantly in the particulate phase, indicating that dust significantly inhibits the partitioning of nitrate into the gaseous
438 phase. In addition, our sensitivity analyses also showed that ammonia reduction had the most significant effect on reducing
439 nitrate aerosols under dust-free conditions. However, the effectiveness of ammonia reductions in lowering nitrate aerosol
440 concentrations was significantly reduced due to the influence of NVCs on nitrate partitioning under dust pollution
441 scenarios. These findings suggest that dust pollution can substantially weaken the impact of ammonia reductions on nitrate
442 aerosol formation, highlighting the need for targeted control strategies during dust storm events. Dust emission remains
443 a significant air pollution concern worldwide, while urban nitrate aerosol pollution is a pressing issue in many cities,
444 particularly in East Asia, where the frequency of natural dust events has increased in recent years. These dust storms,
445 along with anthropogenic dust, can substantially alter aerosol chemistry by modifying aerosol pH and nitrate partitioning.
446 Therefore, effective dust control strategies are critical for mitigating the adverse effects of aerosol acidity on nitrate
447 aerosol formation and improving air quality in dust-prone regions.

448

449 *Data availability.* Additional meteorological parameters can be accessed at the European Centre for Medium-Range
450 Weather Forecasts (ECMWF) ERA5 reanalysis dataset (<https://cds.climate.copernicus.eu/>; last access: 21 November
451 2023). Regional PM₁₀ data can be accessed at the China National Environmental Monitoring Centre
452 (<https://air.cnemc.cn:18007/>; 21 last access: November, 2023). The additional data will be made available upon request
453 (yjzhang@nuist.edu.cn).

455 *Author contributions.*

456 YZ conceived and designed the study. HL and YZ conducted the simulations and data analysis. HL, YZ, SZ, YR, JQ,
457 and MZ carried out field measurements and validated the data. HL and YZ wrote the original manuscript, while DL, FC,
458 OF, HD, and XG provided critical feedback and contributed to the manuscript revisions.

460 *Competing interests.* The authors declare that they have no conflict of interest.

462 *Acknowledgements.*

463 This study was supported by the National Natural Science Foundation of China (grant no. 42207124) and Natural
464 Science Foundation of Jiangsu Province (grant no. BK20210663).

465 **References**

- 466 Beaudor, M., Hauglustaine, D., Lathière, J., Van Damme, M., Clarisse, L., and Vuichard, N.: Evaluating present-day and
467 future impacts of agricultural ammonia emissions on atmospheric chemistry and climate, *EGUsphere*, 2024, 1-40,
468 <https://doi.org/10.5194/egusphere-2024-2022>, 2024.
- 469 Boichu, M., Favez, O., Riffault, V., Petit, J. E., Zhang, Y., Brogniez, C., Sciare, J., Chiapello, I., Clarisse, L., Zhang, S.,
470 Pujol-Söhne, N., Tison, E., Delbarre, H., and Goloub, P.: Large-scale particulate air pollution and chemical fingerprint
471 of volcanic sulfate aerosols from the 2014–2015 Holuhraun flood lava eruption of Bárðarbunga volcano (Iceland),
472 *Atmos. Chem. Phys.*, 19, 14253–14287, <https://doi.org/10.5194/acp-19-14253-2019>, 2019.
- 473 Chen, S., Chen, J., Zhang, Y., Lin, J., Bi, H., Song, H., Chen, Y., Lian, L., Liu, C., and Zhang, R.: Anthropogenic dust:
474 sources, characteristics and emissions, *Environ. Res. Lett.*, 18, 103002, <https://doi.org/10.1088/1748-9326/acf479>,
475 2023a.
- 476 Chen, S., Zhao, D., Huang, J., He, J., Chen, Y., Chen, J., Bi, H., Lou, G., Du, S., Zhang, Y., and Yang, F.: Mongolia
477 Contributed More than 42% of the Dust Concentrations in Northern China in March and April 2023, *Adv. Atmos. Sci.*,
478 40, 1549–1557, <https://doi.org/10.1007/s00376-023-3062-1>, 2023b.
- 479 Chen, S., Jiang, N., Huang, J., Xu, X., Zhang, H., Zang, Z., Huang, K., Xu, X., Wei, Y., Guan, X., Zhang, X., Luo, Y., Hu,
480 Z., and Feng, T.: Quantifying contributions of natural and anthropogenic dust emission from different climatic regions,

Atmos. Environ. , 191, 94-104, <https://doi.org/10.1016/j.atmosenv.2018.07.043>, 2018.

Chen, Y., Chen, S., Zhou, J., Zhao, D., Bi, H., Zhang, Y., Alam, K., Yu, H., Yang, Y., and Chen, J.: A super dust storm enhanced by radiative feedback, *npj Clim. Atmos. Sci.*, 6, 90, <https://doi.org/10.1038/s41612-023-00418-y>, 2023c.

Clegg, S. L., Brimblecombe, P., and Wexler, A. S.: Thermodynamic Model of the System $\text{H}^+ - \text{NH}_4^+ - \text{SO}_4^{2-} - \text{NO}_3^- - \text{H}_2\text{O}$ at Tropospheric Temperatures, *J. Phys. Chem. A*, 102, 2137-2154, <https://doi.org/10.1021/jp973042r>, 1998.

Ding, J., Zhao, P., Su, J., Dong, Q., Du, X., and Zhang, Y.: Aerosol pH and its driving factors in Beijing, *Atmos. Chem. Phys.*, 19, 7939-7954, <https://doi.org/10.5194/acp-19-7939-2019>, 2019.

Duan, J., Huang, R.-J., Wang, Y., Xu, W., Zhong, H., Lin, C., Huang, W., Gu, Y., Ovadnevaite, J., Ceburnis, D., and O'Dowd, C.: Measurement report: Size-resolved secondary organic aerosol formation modulated by aerosol water uptake in wintertime haze, *Atmos. Chem. Phys.*, 24, 7687-7698, <https://doi.org/10.5194/acp-24-7687-2024>, 2024.

Fang, T., Guo, H., Zeng, L., Verma, V., Nenes, A., and Weber, R. J.: Highly Acidic Ambient Particles, Soluble Metals, and Oxidative Potential: A Link between Sulfate and Aerosol Toxicity, *Environ. Sci. Technol.*, 51, 2611-2620, <https://doi.org/10.1021/acs.est.6b06151>, 2017.

Fountoukis, C. and Nenes, A.: ISORROPIA II: a computationally efficient thermodynamic equilibrium model for $\text{K}^+ - \text{Ca}^{2+} - \text{Mg}^{2+} - \text{NH}_4^+ - \text{Na}^+ - \text{SO}_4^{2-} - \text{NO}_3^- - \text{Cl}^- - \text{H}_2\text{O}$ aerosols, *Atmos. Chem. Phys.*, 7, 4639-4659, <https://doi.org/10.5194/acp-7-4639-2007>, 2007.

Fu, X., Wang, S. X., Cheng, Z., Xing, J., Zhao, B., Wang, J. D., and Hao, J. M.: Source, transport and impacts of a heavy dust event in the Yangtze River Delta, China, in 2011, *Atmos. Chem. Phys.*, 14, 1239-1254, <https://doi.org/10.5194/acp-14-1239-2014>, 2014.

Gao, D., Zhao, B., Wang, S., Wang, Y., Gaudet, B., Zhu, Y., Wang, X., Shen, J., Li, S., He, Y., Yin, D., and Dong, Z.: Increased importance of aerosol–cloud interactions for surface $\text{PM}_{2.5}$ pollution relative to aerosol–radiation interactions in China with the anthropogenic emission reductions, *Atmos. Chem. Phys.*, 23, 14359-14373, <https://doi.org/10.5194/acp-23-14359-2023>, 2023.

Geng, G., Zhang, Q., Tong, D., Li, M., Zheng, Y., Wang, S., and He, K.: Chemical composition of ambient $\text{PM}_{2.5}$ over China and relationship to precursor emissions during 2005–2012, *Atmos. Chem. Phys.*, 17, 9187-9203, <https://doi.org/10.5194/acp-17-9187-2017>, 2017.

Goudie, A. S.: Desert dust and human health disorders, *Environ. Int.*, 63, 101-113, <https://doi.org/10.1016/j.envint.2013.10.011>, 2014.

Guo, H., Weber, R. J., and Nenes, A.: High levels of ammonia do not raise fine particle pH sufficiently to yield nitrogen oxide-dominated sulfate production, *Sci. Rep.*, 7, 12109, <https://doi.org/10.1038/s41598-017-11704-0>, 2017a.

Guo, H., Otjes, R., Schlag, P., Kiendler-Scharr, A., Nenes, A., and Weber, R. J.: Effectiveness of ammonia reduction on control of fine particle nitrate, *Atmos. Chem. Phys.*, 18, 12241-12256, <https://doi.org/10.5194/acp-18-12241-2018>, 2018.

Guo, H., Liu, J., Froyd, K. D., Roberts, J. M., Veres, P. R., Hayes, P. L., Jimenez, J. L., Nenes, A., and Weber, R. J.: Fine particle pH and gas–particle phase partitioning of inorganic species in Pasadena, California, during the 2010 CalNex campaign, *Atmos. Chem. Phys.*, 17, 5703-5719, <https://doi.org/10.5194/acp-17-5703-2017>, 2017b.

Guo, H., Sullivan, A. P., Campuzano - Jost, P., Schroder, J. C., Lopez - Hilfiker, F. D., Dibb, J. E., Jimenez, J. L., Thornton, J. A., Brown, S. S., Nenes, A., and Weber, R. J.: Fine particle pH and the partitioning of nitric acid during winter in the northeastern United States, *J. Geophys. Res. Atmos.*, 121, 10,355 - 310,376, <https://doi.org/10.1002/2016JD025311>, 2016.

Guo, H., Xu, L., Bougiatioti, A., Cerully, K. M., Capps, S. L., Hite, J. R., Carlton, A. G., Lee, S. H., Bergin, M. H., Ng, N. L., Nenes, A., and Weber, R. J.: Fine-particle water and pH in the southeastern United States, *Atmos. Chem. Phys.*,

15, 5211-5228, <https://doi.org/10.5194/acp-15-5211-2015>, 2015.

Hauglustaine, D. A., Balkanski, Y., and Schulz, M.: A global model simulation of present and future nitrate aerosols and their direct radiative forcing of climate, *Atmos. Chem. Phys.*, 14, 11031-11063, <https://doi.org/10.5194/acp-14-11031-2014>, 2014.

Hrdina, A., Murphy, J. G., Hallar, A. G., Lin, J. C., Moravek, A., Bares, R., Petersen, R. C., Franchin, A., Middlebrook, A. M., Goldberger, L., Lee, B. H., Baasandorj, M., and Brown, S. S.: The role of coarse aerosol particles as a sink of HNO_3 in wintertime pollution events in the Salt Lake Valley, *Atmos. Chem. Phys.*, 21, 8111-8126, <https://doi.org/10.5194/acp-21-8111-2021>, 2021.

Huang, J., Fu, Q., Zhang, W., Wang, X., Zhang, R., Ye, H., and Warren, S. G.: Dust and Black Carbon in Seasonal Snow Across Northern China, *Bull. Am. Meteorol.*, 92, 175-181, <https://doi.org/10.1175/2010BAMS3064.1>, 2011.

Jickells, T. D., An, Z. S., Andersen, K. K., Baker, A. R., Bergametti, G., Brooks, N., Cao, J. J., Boyd, P. W., Duce, R. A., Hunter, K. A., Kawahata, H., Kubilay, N., laRoche, J., Liss, P. S., Mahowald, N., Prospero, J. M., Ridgwell, A. J., Tegen, I., and Torres, R.: Global Iron Connections Between Desert Dust, Ocean Biogeochemistry, and Climate, *Science*, 308, 67-71, <https://doi.org/10.1126/science.1105959>, 2005.

Kurokawa, J. and Ohara, T.: Long-term historical trends in air pollutant emissions in Asia: Regional Emission inventory in ASia (REAS) version 3, *Atmos. Chem. Phys.*, 20, 12761-12793, [10.5194/acp-20-12761-2020](https://doi.org/10.5194/acp-20-12761-2020), 2020.

Laskin, A., Wietsma, T. W., Krueger, B. J., and Grassian, V. H.: Heterogeneous chemistry of individual mineral dust particles with nitric acid: A combined CCSEM/EDX, ESEM, and ICP - MS study, *J. Geophys. Res. Atmos.*, 110, <https://doi.org/10.1029/2004JD005206>, 2005.

Li, G., Su, H., Zheng, G., Zhou, M., Han, W., Zhang, Y., Ma, N., Wang, H., Klimach, T., and Cheng, Y.: Novel Device for in Situ and Real-Time Detection of the Acidity of Ambient Aerosols: Laboratory Characterization and Ambient Measurements, *Environ. Sci. Technol.*, 59, 659-667, <https://doi.org/10.1021/acs.est.4c09221>, 2025.

Li, J., Zhang, N., Tian, P., Zhang, M., Shi, J., Chang, Y., Zhang, L., Liu, Z., and Wang, Y.: Significant roles of aged dust aerosols on rapid nitrate formation under dry conditions in a semi-arid city, *Environmental Pollution*, 336, 122395, <https://doi.org/10.1016/j.envpol.2023.122395>, 2023.

Li, W. J. and Shao, L. Y.: Observation of nitrate coatings on atmospheric mineral dust particles, *Atmos. Chem. Phys.*, 9, 1863-1871, <https://doi.org/10.5194/acp-9-1863-2009>, 2009.

Liu, X., Song, H., Lei, T., Liu, P., Xu, C., Wang, D., Yang, Z., Xia, H., Wang, T., and Zhao, H.: Effects of natural and anthropogenic factors and their interactions on dust events in Northern China, *Catena*, 196, 104919, <https://doi.org/10.1016/j.catena.2020.104919>, 2021.

Liu, Y., Zhan, J., Zheng, F., Song, B., Zhang, Y., Ma, W., Hua, C., Xie, J., Bao, X., Yan, C., Bianchi, F., Petäjä, T., Ding, A., Song, Y., He, H., and Kulmala, M.: Dust emission reduction enhanced gas-to-particle conversion of ammonia in the North China Plain, *Nat. Commun.*, 13, 6887, <https://doi.org/10.1038/s41467-022-34733-4>, 2022.

Lundberg, S. M. and Lee, S.-I.: A unified approach to interpreting model predictions, *Proceedings of the 31st International Conference on Neural Information Processing Systems*, Long Beach, California, USA, <https://doi.org/10.48550/arXiv.1705.07874>, 2017.

Mahowald, N. M., Muhs, D. R., Levis, S., Rasch, P. J., Yoshioka, M., Zender, C. S., and Luo, C.: Change in atmospheric mineral aerosols in response to climate: Last glacial period, preindustrial, modern, and doubled carbon dioxide climates, *J. Geophys. Res. Atmos.*, 111, <https://doi.org/10.1029/2005JD006653>, 2006.

Malm, W. C. and Day, D. E.: Estimates of aerosol species scattering characteristics as a function of relative humidity, *Atmospheric Environment*, 35, 2845-2860, [https://doi.org/10.1016/S1352-2310\(01\)00077-2](https://doi.org/10.1016/S1352-2310(01)00077-2), 2001.

Metzger, S., Dentener, F., Pandis, S., and Lelieveld, J.: Gas/aerosol partitioning: 1. A computationally efficient model, *J.*

Geophys. Res. Atmos., 107, <https://doi.org/10.1029/2001JD001102>, 2002.

Milousis, A., Klingmüller, K., Tsimpidi, A. P., Kok, J. F., Kanakidou, M., Nenes, A., and Karydis, V. A.: Impact of mineral dust on the global nitrate aerosol direct and indirect radiative effect, *Atmos. Chem. Phys.*, 1579, <https://doi.org/10.5194/egusphere-2024-1579>, 2024.

Nah, T., Guo, H., Sullivan, A. P., Chen, Y., Tanner, D. J., Nenes, A., Russell, A., Ng, N. L., Huey, L. G., and Weber, R. J.: Characterization of aerosol composition, aerosol acidity, and organic acid partitioning at an agriculturally intensive rural southeastern US site, *Atmos. Chem. Phys.*, 18, 11471-11491, <https://doi.org/10.5194/acp-18-11471-2018>, 2018.

Nenes, A., Pandis, S. N., Weber, R. J., and Russell, A.: Aerosol pH and liquid water content determine when particulate matter is sensitive to ammonia and nitrate availability, *Atmos. Chem. Phys.*, 20, 3249-3258, <https://doi.org/10.5194/acp-20-3249-2020>, 2020.

Nenes, A., Pandis, S. N., Kanakidou, M., Russell, A. G., Song, S., Vasilakos, P., and Weber, R. J.: Aerosol acidity and liquid water content regulate the dry deposition of inorganic reactive nitrogen, *Atmos. Chem. Phys.*, 21, 6023-6033, <https://doi.org/10.5194/acp-21-6023-2021>, 2021.

Nguyen, T. B., Coggon, M. M., Bates, K. H., Zhang, X., Schwantes, R. H., Schilling, K. A., Loza, C. L., Flagan, R. C., Wennberg, P. O., and Seinfeld, J. H.: Organic aerosol formation from the reactive uptake of isoprene epoxydiols (IEPOX) onto non-acidified inorganic seeds, *Atmos. Chem. Phys.*, 14, 3497-3510, <https://doi.org/10.5194/acp-14-3497-2014>, 2014.

Notaro, M., Yu, Y., and Kalashnikova, O. V.: Regime shift in Arabian dust activity, triggered by persistent Fertile Crescent drought, *J. Geophys. Res. Atmos.*, 120, 10,229-210,249, <https://doi.org/10.1002/2015JD023855>, 2015.

Petit, J.-E., Favez, O., Albinet, A., and Canonaco, F.: A user-friendly tool for comprehensive evaluation of the geographical origins of atmospheric pollution: Wind and trajectory analyses, *Environ. Model. Softw.*, 88, 183-187, <https://doi.org/10.1016/j.envsoft.2016.11.022>, 2017.

Rosenfeld, D., Rudich, Y., and Lahav, R.: Desert dust suppressing precipitation: A possible desertification feedback loop, *Proc. Natl. Acad. Sci. U.S.A.*, 98, 5975-5980, <https://doi.org/10.1073/pnas.101122798>, 2001.

Rumsey, I. C., Cowen, K. A., Walker, J. T., Kelly, T. J., Hanft, E. A., Mishoe, K., Rogers, C., Proost, R., Beachley, G. M., Lear, G., Frelink, T., and Otjes, R. P.: An assessment of the performance of the Monitor for AeRosols and GAses in ambient air (MARGA): a semi-continuous method for soluble compounds, *Atmos. Chem. Phys.*, 14, 5639-5658, <https://doi.org/10.5194/acp-14-5639-2014>, 2014.

Schaap, M., Spindler, G., Schulz, M., Acker, K., Maenhaut, W., Berner, A., Wieprecht, W., Streit, N., Müller, K., Brüggemann, E., Chi, X., Putaud, J. P., Hitzengerger, R., Puxbaum, H., Baltensperger, U., and ten Brink, H.: Artefacts in the sampling of nitrate studied in the “INTERCOMP” campaigns of EUROTRAC-AEROSOL, *Atmos. Environ.*, 38, 6487-6496, <https://doi.org/10.1016/j.atmosenv.2004.08.026>, 2004.

Seinfeld, J. H., Pandis, S. N., and Noone, K. J.: Atmospheric Chemistry and Physics: From Air Pollution to Climate Change, *Physics Today*, 51, 88-90, <https://www.wiley.com/en-cn/9781118947401>, 1998.

Shao, Y. and Dong, C. H.: A review on East Asian dust storm climate, modelling and monitoring, *Glob. Planet. Change*, 52, 1-22, <https://doi.org/10.1016/j.gloplacha.2006.02.011>, 2006.

Shi, X., Nenes, A., Xiao, Z., Song, S., Yu, H., Shi, G., Zhao, Q., Chen, K., Feng, Y., and Russell, A. G.: High-Resolution Data Sets Unravel the Effects of Sources and Meteorological Conditions on Nitrate and Its Gas-Particle Partitioning, *Environ. Sci. Technol.*, 53, 3048-3057, <https://doi.org/10.1021/acs.est.8b06524>, 2019.

Song, C. H., Carmichael, G. R.: Gas-Particle Partitioning of Nitric Acid Modulated by Alkaline Aerosol, *J. Atmos. Chem.*, 40, 1-22, <https://doi.org/10.1023/A:1010657929716>, 2001.

Song, X., Wang, Y., Huang, X., Wang, Y., Li, Z., Zhu, B., Ren, R., An, J., Yan, J., Zhang, R., Shang, Y., and Zhan, P.: The

607 Impacts of Dust Storms With Different Transport Pathways on Aerosol Chemical Compositions and Optical
608 Hygroscopicity of Fine Particles in the Yangtze River Delta, *J. Geophys. Res. Atmos.*, 128, 10.1029/2023jd039679,
609 2023.

610 Soussé-Villa, R., Jorba, O., Gonçalves Ageitos, M., Bowdalo, D., Guevara, M., and Pérez García-Pando, C.: A
611 Comprehensive Global Modelling Assessment of Nitrate Heterogeneous Formation on Desert Dust, *EGUsphere*, 2024,
612 1-53, <https://doi.org/10.5194/egusphere-2024-2310>, 2024.

613 Stelson, A. W. and Seinfeld, J. H.: Relative humidity and temperature dependence of the ammonium nitrate dissociation
614 constant, *Atmos. Environ.*, 16, 983-992, [https://doi.org/10.1016/0004-6981\(82\)90184-6](https://doi.org/10.1016/0004-6981(82)90184-6), 1982.

615 Sun, J., Zhang, M., and Liu, T.: Spatial and temporal characteristics of dust storms in China and its surrounding regions,
616 1960–1999: Relations to source area and climate, *J. Geophys. Res. Atmos.*, 106, 10325-10333,
617 <https://doi.org/10.1029/2000JD900665>, 2001.

618 Tan, S.-C., Shi, G.-Y., and Wang, H.: Long-range transport of spring dust storms in Inner Mongolia and impact on the
619 China seas, *Atmos. Environ.*, 46, 299-308, <https://doi.org/10.1016/j.atmosenv.2011.09.058>, 2012.

620 Tobo, Y., Zhang, D., Matsuki, A., and Iwasaka, Y.: Asian dust particles converted into aqueous droplets under remote
621 marine atmospheric conditions, *Proc. Natl. Acad. Sci. U.S.A.*, 107, 17905-17910,
622 <https://doi.org/10.1073/pnas.1008235107>, 2010.

623 Trebs, I., Meixner, F. X., Slanina, J., Otjes, R., Jongejan, P., and Andreae, M. O.: Real-time measurements of ammonia,
624 acidic trace gases and water-soluble inorganic aerosol species at a rural site in the Amazon Basin, *Atmos. Chem. Phys.*,
625 4, 967-987, <https://doi.org/10.5194/acp-4-967-2004>, 2004.

626 Vasilakos, P., Russell, A., Weber, R., and Nenes, A.: Understanding nitrate formation in a world with less sulfate, *Atmos.*
627 *Chem. Phys.*, 18, 12765-12775, <https://doi.org/10.5194/acp-18-12765-2018>, 2018.

628 Wang, G., Zhang, R., Gomez, M. E., Yang, L., Levy Zamora, M., Hu, M., Lin, Y., Peng, J., Guo, S., Meng, J., Li, J.,
629 Cheng, C., Hu, T., Ren, Y., Wang, Y., Gao, J., Cao, J., An, Z., Zhou, W., Li, G., Wang, J., Tian, P., Marrero-Ortiz, W.,
630 Secrest, J., Du, Z., Zheng, J., Shang, D., Zeng, L., Shao, M., Wang, W., Huang, Y., Wang, Y., Zhu, Y., Li, Y., Hu, J.,
631 Pan, B., Cai, L., Cheng, Y., Ji, Y., Zhang, F., Rosenfeld, D., Liss, P. S., Duce, R. A., Kolb, C. E., and Molina, M. J.:
632 Persistent sulfate formation from London Fog to Chinese haze, *Proc. Natl. Acad. Sci. U.S.A.*, 113, 13630-13635,
633 <https://doi.org/10.1073/pnas.1616540113>, 2016.

634 Wang, J., Gui, H., An, L., Hua, C., Zhang, T., and Zhang, B.: Modeling for the source apportionments of PM10 during
635 sand and dust storms over East Asia in 2020, *Atmos. Environ.*, 267, 118768,
636 <https://doi.org/10.1016/j.atmosenv.2021.118768>, 2021.

637 Wang, T., Liu, Y., Cheng, H., Wang, Z., Fu, H., Chen, J., and Zhang, L.: Significant formation of sulfate aerosols
638 contributed by the heterogeneous drivers of dust surface, *Atmos. Chem. Phys.*, 22, 13467-13493,
639 <https://doi.org/10.5194/acp-22-13467-2022>, 2022.

640 Weber, R. J., Guo, H., Russell, A. G., and Nenes, A.: High aerosol acidity despite declining atmospheric sulfate
641 concentrations over the past 15 years, *Nat. Geosci.*, 9, 282-285, <https://doi.org/10.1038/ngeo2665>, 2016.

642 Xie, Y., Wang, G., Wang, X., Chen, J., Chen, Y., Tang, G., Wang, L., Ge, S., Xue, G., Wang, Y., and Gao, J.: Nitrate-
643 dominated PM2.5 and elevation of particle pH observed in urban Beijing during the winter of 2017, *Atmos. Chem.*
644 *Phys.*, 20, 5019-5033, <https://doi.org/10.5194/acp-20-5019-2020>, 2020.

645 Xin, K., Chen, J., and Tseren-Ochir, S.-E.: Formation mechanism and source apportionment of nitrate in atmospheric
646 aerosols, *APN Sci. Bull.*, 13, 102-111, <https://doi.org/10.30852/sb.2023.2225>, 2023.

647 Xu, J. W., Lin, J., Luo, G., Adeniran, J., and Kong, H.: Foreign emissions exacerbate PM2.5 pollution in China through
648 nitrate chemistry, *Atmos. Chem. Phys.*, 23, 4149-4163, <https://doi.org/10.5194/acp-23-4149-2023>, 2023.

649 Xu, L., Fukushima, S., Sobanska, S., Murata, K., Naganuma, A., Liu, L., Wang, Y., Niu, H., Shi, Z., Kojima, T., Zhang,
 650 D., and Li, W.: Tracing the evolution of morphology and mixing state of soot particles along with the movement of an
 651 Asian dust storm, *Atmos. Chem. Phys.*, 20, 14321-14332, <https://doi.org/10.5194/acp-20-14321-2020>, 2020.

652 Xu, L., Guo, H., Boyd, C. M., Klein, M., Bougiatioti, A., Cerully, K. M., Hite, J. R., Isaacman-VanWertz, G., Kreisberg,
 653 N. M., Knote, C., Olson, K., Koss, A., Goldstein, A. H., Hering, S. V., de Gouw, J., Baumann, K., Lee, S.-H., Nenes,
 654 A., Weber, R. J., and Ng, N. L.: Effects of anthropogenic emissions on aerosol formation from isoprene and
 655 monoterpenes in the southeastern United States, *Proc. Natl. Acad. Sci. U.S.A.*, 112, 37-42,
 656 <https://doi.org/10.1073/pnas.1417609112>, 2015.

657 Zhai, S., Jacob, D. J., Wang, X., Liu, Z., Wen, T., Shah, V., Li, K., Moch, J. M., Bates, K. H., Song, S., Shen, L., Zhang,
 658 Y., Luo, G., Yu, F., Sun, Y., Wang, L., Qi, M., Tao, J., Gui, K., Xu, H., Zhang, Q., Zhao, T., Wang, Y., Lee, H. C., Choi,
 659 H., and Liao, H.: Control of particulate nitrate air pollution in China, *Nat. Geosci.*, 14, 389-395,
 660 <https://doi.org/10.1038/s41561-021-00726-z>, 2021.

661 Zhang, C., Yan, M., Du, H., Ban, J., Chen, C., Liu, Y., and Li, T.: Mortality risks from a spectrum of causes associated
 662 with sand and dust storms in China, *Nat. Commun.*, 14, 6867, <https://doi.org/10.1038/s41467-023-42530-w>, 2023.

663 Zhang, R., Wang, G., Guo, S., Zamora, M. L., Ying, Q., Lin, Y., Wang, W., Hu, M., and Wang, Y.: Formation of Urban
 664 Fine Particulate Matter, *Chem. Rev.*, 115, 3803-3855, <https://doi.org/10.1021/acs.chemrev.5b00067>, 2015.

665 Zhang, Y., Tang, L., Sun, Y., Favez, O., Canonaco, F., Albinet, A., Couvidat, F., Liu, D., Jayne, J. T., Wang, Z., Croteau,
 666 P. L., Canagaratna, M. R., Zhou, H.-c., Prévôt, A. S. H., and Worsnop, D. R.: Limited formation of isoprene epoxydiols-
 667 derived secondary organic aerosol under NO_x-rich environments in Eastern China, *Geophys. Res. Lett.*, 44, 2035-2043,
 668 <https://doi.org/10.1002/2016GL072368>, 2017.

669 Zhao, X., Huang, K., Fu, J. S., and Abdullaev, S. F.: Long-range transport of Asian dust to the Arctic: identification of
 670 transport pathways, evolution of aerosol optical properties, and impact assessment on surface albedo changes, *Atmos.*
 671 *Chem. Phys.*, 22, 10389-10407, <https://doi.org/10.5194/acp-22-10389-2022>, 2022.

672 Zheng, B., Cheng, J., Geng, G., Wang, X., Li, M., Shi, Q., Qi, J., Lei, Y., Zhang, Q., and He, K.: Mapping anthropogenic
 673 emissions in China at 1 km spatial resolution and its application in air quality modeling, *Sci. Bull.*, 66, 612-620,
 674 <https://doi.org/10.1016/j.scib.2020.12.008>, 2021.

675 Zheng, G., Su, H., Wang, S., Andreae, M. O., Pöschl, U., and Cheng, Y.: Multiphase buffer theory explains contrasts in
 676 atmospheric aerosol acidity, *Science*, 369, 1374-1377, <https://doi.org/10.1126/science.aba3719>, 2020.

677 Zheng, M., Xu, K., Yuan, L., Chen, N., and Cao, M.: Fine Particle pH and its Impact on PM_{2.5} Control in a Megacity of
 678 Central China, *Aerosol and Air Quality Research*, 22, <https://doi.org/10.4209/aaqr.210394>, 2022.

679 Zhi, M., Wang, G., Xu, L., Li, K., Nie, W., Niu, H., Shao, L., Liu, Z., Yi, Z., Wang, Y., Shi, Z., Ito, A., Zhai, S., and Li,
 680 W.: How Acid Iron Dissolution in Aged Dust Particles Responds to the Buffering Capacity of Carbonate Minerals
 681 during Asian Dust Storms, *Environ. Sci. Technol.*, <https://doi.org/10.1021/acs.est.4c12370>, 2025.

682 Zhu, W., Qi, Y., Tao, H., Zhang, H., Li, W., Qu, W., Shi, J., Liu, Y., Sheng, L., Wang, W., Wu, G., Zhao, Y., Zhang, Y.,
 683 Yao, X., Wang, X., Yi, L., Ma, Y., and Zhou, Y.: Investigation of a haze-to-dust and dust swing process at a coastal city
 684 in northern China part I: Chemical composition and contributions of anthropogenic and natural sources, *Sci. Total*
 685 *Environ.*, 851, 158270, <https://doi.org/10.1016/j.scitotenv.2022.158270>, 2022.

686